Journal of Biomedical Optics

BiomedicalOptics.SPIEDigitalLibrary.org

Mesoscopic reflectance angular domain spectroscopic imaging

Yan Zhang
Fartash Vasefi
Eldon Ng
Astrid Chamson-Reig
Bozena Kaminska
Jeffrey J. L. Carson

SPIE.

Mesoscopic reflectance angular domain spectroscopic imaging

Yan Zhang,[a] Fartash Vasefi,[a,b] Eldon Ng,[b,c] Astrid Chamson-Reig,[b] Bozena Kaminska,[a] and Jeffrey J. L. Carson[b,c,*]
[a]Simon Fraser University, School of Engineering Science, Burnaby, British Columbia V5S 1S6, Canada
[b]Lawson Health Research Institute, Imaging Program, St. Joseph's Health Care, London, Ontario N6A 4V2, Canada
[c]University of Western Ontario, Schulich School of Medicine and Dentistry, Department of Medical Biophysics, London, Ontario N6A 3K7, Canada

Abstract. The advancement of angular domain imaging in mesoscopic reflectance multispectral imaging is reported. The key component is an angular filter array that performs the angular filtration of the back-scattered photons and generates image contrast due to the variances in tissue optical properties. The proposed modality enables multispectral imaging of subsurface features for samples too thick for transillumination angular domain spectroscopic imaging (ADSI) approaches. The validation was carried out with tissue-mimicking phantoms with multiple absorptive features embedded below the surface. Multispectral images in the range of 666 to 888 nm clearly revealed the location of the features with the background scattering levels up to 20 cm^{-1}. The shape of the features was recoverable at depths of up to three to four times the transport mean free path. The spatial resolution was <1 mm and the field-of-view was larger than 2.5 cm × 3.0 cm. Furthermore, the attenuation spectra of measured absorptive features were successfully extracted. Target detectability and imaging quality with different background scattering levels, target depths, and illumination focal depths were discussed, as well as the capability of ADSI in reflectance optical mesoscopic imaging and its potential applications. [DOI: 10.1117/1.JBO.19.7.076010]

Keywords: imaging system; multispectral and hyperspectral imaging; mesoscopic imaging; spectroscopy; tissue imaging; angular domain imaging; tissue mimicking phantoms.

Paper 130637PRR received Aug. 30, 2013; revised manuscript received May 17, 2014; accepted for publication May 22, 2014; published online Jul. 14, 2014.

1 Introduction

1.1 *Angular Domain Imaging*

This paper reports our recent development of angular domain imaging (ADI) and angular domain spectroscopic imaging (ADSI) within the context of mesoscopic reflectance imaging. ADI modalities detect optical contrast from targets embedded in a turbid medium via trajectory filtration of light. Angular filtration greatly improves the resolution and contrast of the resultant images and is performed in practice with an angular filter array (AFA).[1–3] The AFA consists of an array of parallel microchannels. The aspect ratio of each microchannel (length/width) determines the acceptance angle, which is typically <0.5 deg for AFAs of practical use.[1–6] The AFA selects image-bearing quasiballistic photons that travel within the acceptance angle of the device and rejects image-degrading scattered photons. Although angular filtration of photons can be performed with a lens-based system, AFA-based ADI is more robust against spatial resolution degradation at larger depths.[5] Furthermore, the angular filtration function of the AFA is largely independent of wavelength, which enables spectroscopic analysis by ADSI.[2]

Both ADI and ADSI were developed to image turbid media such as biological tissues. So far, most work has been with transillumination configurations for multispectral and hyperspectral analysis,[2] fluorescence,[5] and computed tomography.[6] The techniques have been successfully applied to small animal imaging and tissue characterization. Examples include fluorescence imaging of the vertebral structure of a hairless mouse and hyperspectral image identification of the tumor tissue in murine models and human breast surgical samples.[2,5,7]

1.2 *Reflectance ADI*

In general, reflectance-based systems are popular for noninvasive optical imaging due to the impracticalities of transillumination imaging of optically thick tissue sections. Reflectance-based systems utilize detection optics positioned on the same side of the sample as the illumination optics. The arrangement facilitates the detection of structures near the surface, mitigating information loss and resolution degradation that occur when attempting to traverse an extended optical path. The first demonstration of reflectance ADI utilized a laser to illuminate subsurface objects from behind using the inherent scatter within the turbid medium ($\mu_s' \sim 5$ cm^{-1}).[4] Images were acquired by step-scanning the sample across the AFA and stacking the one-dimensional line profiles captured at the AFA output at each step. For typical AFA geometries and scan protocols, targets embedded 1 to 3 mm below the surface were resolved with sub-millimeters spatial resolution across a field-of-view of several square centimeters. In comparison to other optical modalities, reflectance ADI offers poorer spatial resolution than optical coherence tomography, confocal microscopy (CM), two or multiphoton (2P/MP) excitation microscopy, and speckle imaging.[8–15] However, reflectance ADI offers better resolution than

*Address all correspondence to: Jeffrey J. L. Carson, E-mail: jcarson@lawsonimaging.ca

0091-3286/2014/$25.00

diffuse optical tomography (DOT) for near-surface objects without the need for inversion-based image reconstruction.[8,9,16,17]

1.3 *Reflectance Optical Imaging in the Mesoscopic Domain*

The development of reflectance-based optical modalities for biomedical imaging in the mesoscopic domain is driven by the need for higher spatial resolution, larger fields-of-view, and deeper imaging depth. Applications[18–32] include (i) the visualization of cellular components in tissues *in vivo* to understand the dynamic interactions of cellular processes at different system levels, (ii) the optical interrogation of molecular and functional changes in intact living organisms in disease progression and treatment study (i.e., skin cancer research and skin oxygenation studies in diabetic patients), (iii) the diagnosis of burn depth and area to predict wound healing, and (iv) the study of organisms for which conventional microscopic or macroscopic imaging modalities are not suitable due to their size, such as insects, animal embryos, and small animal extremities. In the last case, modalities designed for imaging in the microscopic domain do not provide sufficient depth penetration with a sufficient field-of-view without substantial modification to the specimen (e.g., chemical treatment of the specimen to reduce scattering through optical clearing of the specimen), and reflectance modalities designed for imaging in the macroscopic domain may not be applicable due to violation of boundary conditions or approximations during image recovery.[18,31]

The main performance differences between modalities designed for imaging within the microscopic, mesoscopic, or macroscopic domains relate to the transport and attenuation of light in tissue (i.e., scatter and absorption). In biological tissues, depth penetration is closely related to the mean free path (MFP) and transport mean free path (TMFP).[18] The TMFP takes the forward scattering properties of biological tissue into consideration, while MFP does not. The TMFP is determined by the reduced scattering coefficient. Due to the high anisotropic factor of biological tissues, the TMFP is significantly longer than the MFP and ranges from 0.5 to 1.0 mm in most biological soft tissues.[18] Most reported reflectance imaging modalities designed for imaging in the microscopic domain are limited to within 1 TMFP below the surface and the field-of-view is at most a few square millimeters; however, spatial resolution can be submicrometers (i.e., CM and 2P excitation microscopy).[8–15] Imaging modalities designed to operate in the macroscopic domain typically work with deeper targets (>10 TMFP or >1 cm). For these methods, the spatial resolution is on the order of millimeters to centimeters, but with a larger field-of-view capable of imaging the full body of a small animal or substantial regions of human organs such as the brain.[8,9,16–18,30–32]

Most available reflectance-based modalities designed to image in the mesoscopic domain are still in the early stage of development, but are capable of imaging objects embedded in tissues of thickness between 1× and 10× the TMFP and providing submillimeters spatial resolution with a field-of-view of a few square centimeters.[18–20] Laminar optical tomography (LOT),[22,23] spatial frequency domain imaging (SFDI),[24–26] multispectral optoacoustic tomography (MSOT),[27,28,30,32] and back-directional gated spectroscopic imaging (BGSI)[19,21] are excellent examples of modalities capable of imaging in the mesoscopic domain. Both LOT and SFDI represent an extension of DOT that utilizes microscopy hardware or a spatial modulator, respectively. However, unlike algorithms based on diffusion approximation used for DOT, LOT employs reconstruction algorithms that account for source–detector separations that are on the order of the tissue's scattering length[22] and SFDI employs the spatial modulation transfer function from the light diffusion within the tissue to construct the final image.[25] Imaging in the mesoscopic domain with MSOT is derived from either macroscopic or microscopic optoacoustic imaging modalities. The shift from macroscopic optoacoustic imaging to mesoscopic imaging can be achieved by using different photon propagation assumptions, and detectors of higher central frequency and wider bandwidth (10 to 80 MHz) to improve the spatial resolution.[30] Similarly, the shift from microscopic optoacoustic imaging methods such as functional photoacoustic microscopy is also possible. However, the spatial resolution degrades. The image contrast of MSOT is provided by either tissue-intrinsic, such as hemoglobin, or exogenous imaging agents, such as fluorescent dyes. The MSOT specimens are illuminated by multiprojection laser sources and an inversion-based image reconstruction process is required.[27,28,30,32] The BGSI tries to maintain spatial resolution when imaging deeper objects via a $4f$ lens system and an aperture to select information-bearing photons, and by using the weight summation from multiple wavelengths to improve the imaging quality.[21] The reported experiments were performed with a series of phantoms with different anisotropic coefficients and strong absorbers (i.e., color targets or Hb solutions with high Hb concentrations, 100 mg/mL).[19,21] Reflectance ADSI targets to provide the similar imaging capabilities such as the listed modalities above. Besides the imaging capabilities, the setup cost and complexity, data processing requirements, multispectral/hyperspectral compatibility, and time consumption are the other factors to be considered in the actual applications.

1.4 *Objective*

The first objective of the our work was to validate whether AFA-based reflectance ADI was able to perform mesoscopic imaging with submillimeters spatial resolution at depths beyond 1 TMFP with a field-of-view of several square centimeters. The performance of reflectance ADI was measured on tissue-mimicking solid phantoms characteristic of human skin, and spectrally coded absorption targets [indocyanine green (ICG)] at different depths and scattering levels. The second objective was to incorporate the multispectral capability into reflectance ADI at the first time. The third objective was to test the effect of improved illumination and image postprocessing techniques on reflectance ADI performance. The achieved results will be compared to other reflectance optical mesoscopic imaging modalities.

2 Methods

2.1 *Preparation of Tissue-Mimicking Phantoms*

A series of tissue-mimicking phantoms were employed in this project to overcome the reproducibility issues with milk-based scattering media in the previous experiments.[4] In addition, instead of using metal targets as in the previous experiments, the absorption targets were fabricated with ICG, which is an FDA-approved cyanine dye commonly used for cardiac, hepatic, and ophthalmic angiography. Samples were fabricated using procedures developed previously (see Ref. 2). Briefly, each phantom was cast in a plastic mold using mixtures of ICG (I2633-25MG, Sigma Chemical Co., St. Louis,

Missouri), Intralipid® (20%, Fresenius, Kabi AB, Uppsala, Sweden), and agarose (A-6013, Sigma Chemical Co., St. Louis, Missouri). The mold produced six homogeneous targets, which are 3 mm in diameter embedded in a background gel material. The background gel was formed from a mixture of Intralipid® and agarose. The targets were organized into two columns and three rows. Depths of the targets with respect to the front surface of the phantom were arranged by row and were 1, 2, and 3 mm [Figs. 1(a) and 1(b)].

Targets were prepared by first dissolving agarose powder in a phosphate-buffered saline (PBS) solution at an elevated temperature. The target concentration of agarose was 1.0 wt. %. The solution was allowed to cool to at least 56°C before the addition of ICG and Intralipid® and maintained at 50°C in a water bath to prevent hardening of the gel (hardening typically occurred in the range of 32°C to 40°C) before injection into the mold. The location and size of the targets were known due to precise knowledge of the mold geometry in combination with precise knowledge of the camera pixel size and the location of the phantom edges within the field-of-view of the camera. ICG was added to achieve a final concentration of 20 μM. Intralipid® concentration ranged from 0.7 to 2.0 wt. % for the different phantom targets. The mixture was finally transferred into the mold using a 25AWG needle to form six spherical targets. Once the targets hardened (at room temperature), a separately prepared background mixture containing 2.0 wt. % agarose in PBS and the same concentration of Intralipid® as used for the targets was poured into the phantom mold to create the body of the phantom around the targets. The phantom was left to harden at room temperature and was removed from the mold prior to imaging.

2.2 *Optical Properties of Tissue-Mimicking Phantoms*

The absorption coefficient (μ_a) and scattering coefficient (μ_s) of Intralipid® have been shown to be close to the absorption and scattering coefficients of biological tissues.[33–35] Intralipid® has a scattering asymmetry factor (g) of 0.75 ± 0.18 and a μ_s of 362 cm^{-1} for 10 wt. % that is proportional to concentration.[33–35] The absorption coefficient of 10 wt. % Intralipid® has been shown to be on the order of 10^{-1} to 10^{-2} cm^{-1} (between 600 and 950 nm).[33,35] Therefore, the attenuation of light by a gel composed of Intralipid® and agarose is primarily

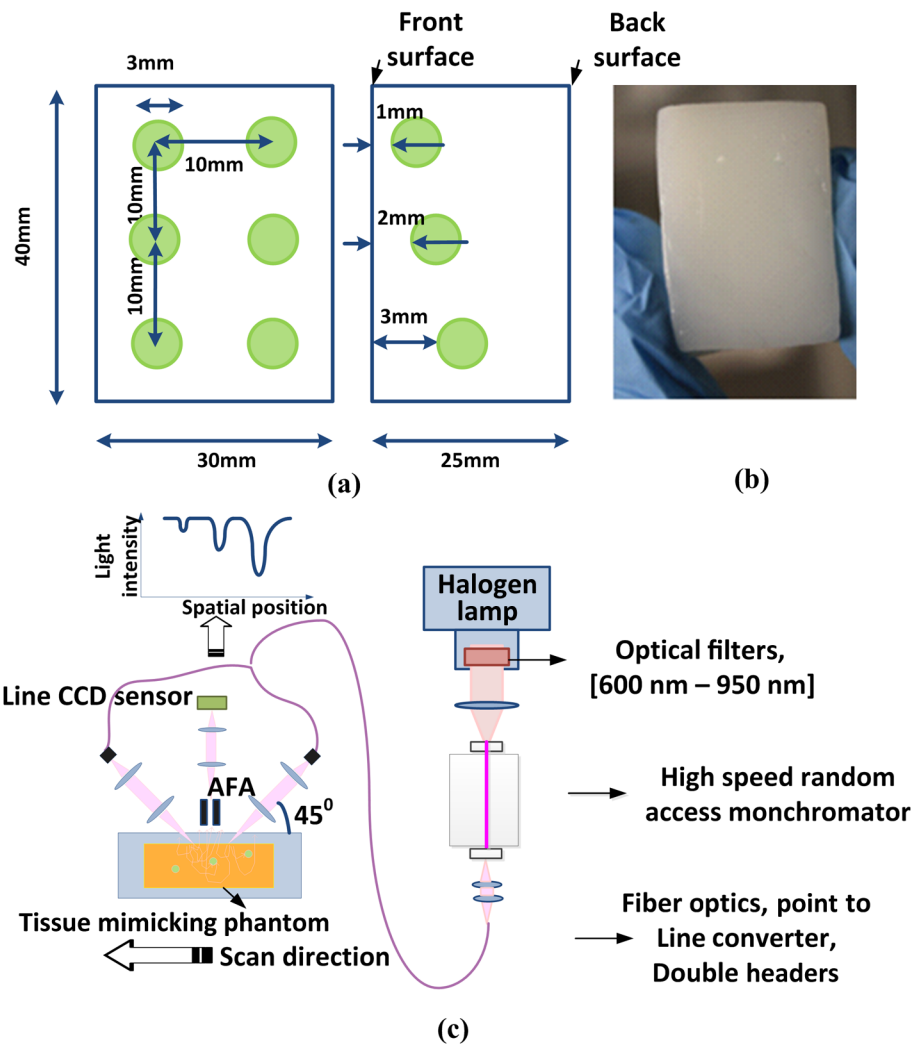

Fig. 1 (a) Front and side views of the phantom showing the location of the targets relative to the surface. (b) The appearance of tissue mimicking-phantom (front surface). (c) Experimental setup for reflectance angular domain spectroscopic imaging.

due to scattering. Using the same reference sources, the equivalent reduced scattering coefficient (μ_s') for Intralipid® was computed to be 6 and 20 cm^{-1} at a concentration of 0.7 and 2.0 wt. %, respectively. Using a spectrophotometer (DU 640, Beckman, Brea, California), the total attenuation of a 1-cm thick cuvette filled with 0.5 wt. % Intralipid® and 2.0 wt. % agarose was measured as 2.5 OD. Assuming that the light loss was primarily due to the optical scatter, the spectrophotometer result suggested that the reduced scattering coefficient was approximately 8.1 cm^{-1} for 0.7 wt. % Intralipid®, consistent with the estimated value from published sources.[33,35,36]

The total attenuation of ICG in 1.0 wt. % agarose solution after a 1 cm optical path was measured previously.[2] Light absorption was observed to be significant between 650 and 820 nm with an attenuation coefficient of 7.0 cm^{-1} at 780 nm for a 20 μM ICG solution. The spectra were similar to data presented in Ref. 37, where the reported absorption coefficient for 20 μM ICG in water was ~2 cm^{-1} at the peak.

2.3 *Experiment Setup*

Figure 1(c) illustrates the reflectance ADSI system. It consisted of a broadband light source (quartz tungsten halogen lamp 50 W; Oriel, Stratford, Connecticut), a near-infrared bandpass filter, which was the combination of a longpass filter (645 nm, Part # 65.1365, Rolyn Optics Co., Covina, California) and a shortpass filter (950 nm, 950FL07-50S, LOT-Oriel GmbH, Darmstadt, Germany), a high speed random access monochromator (Delta Ram V; PTI, Birmingham, New Jersey), two line illuminators, a high-precision sample control stage (ILS250PP; Newport, Irvine, California), an AFA (described below), and a line camera (TCE 1304; 8 μm × 200 μm pixel size; 3648 pixels; Mightex Systems, Toronto, Ontario, Canada). The system was assembled using cage components (Thorlabs; Newton, New Jersey). In operation, the output beam of the QTH lamp was filtered by the near-infrared filter selecting light in the band between 645 and 950 nm. The high speed random access monochromator then selected light in a specific band with the full-width at half-maximum (FWHM) of 30 nm. The beam at the output of the high speed random access monochromator was coupled into a bifurcated fiber optic line illuminator (QDF type; NA 0.55; Dolan-Jenner; Boxborough, Massachusetts). Each line of illumination was focused onto the front surface of the tissue-mimicking phantom via an achromatic lens ($f = 75$ mm, 650 to 1050 nm, 2-in. diameter). The depth of the focal point was adjustable, ranging from the phantom front surface to 4.5 mm below the phantom front surface. The projection angles were 45 and −45 deg with respect to the direction normal to the front surface of the phantom. The distance between the centers of the two incident beams at the phantom front surface was 11 mm, disregarding the depth of the focal point. The phantom was placed on the high-precision stage. During the experiment, the stage was shifted along the y-axis at 0.2 mm/step.

The AFA has been described in detail elsewhere.[5] Briefly, the AFA had 200 parallel channels, where the length of each channel was 10 mm and the maximum acceptance angle of each channel was 0.23 deg. The aperture of each channel was 80 μm × 80 μm and the interchannel wall thickness was 20 μm. The AFA channel periodicity was 100 μm. The length of the AFA in the x-direction was 2.5 cm. The AFA was placed in the center of the apparatus between the two illumination arms and 5.5 mm away from the front surface of the phantom. Since the long axis of each AFA channel was normal to the phantom surface, the AFA only accepted back-illuminated photons, which were emitted in a direction perpendicular to the phantom surface.

Photons that managed to exit the AFA were captured by an optics system (1 in. cage) and were focused onto the CCD line camera. The camera was sensitive over the wavelength range from 350 to 1000 nm and its exposure time was adjustable.

2.4 *Image Capture and Restoration*

The goal of imaging restoration is to detect the existence of absorptive features. A line image was captured by the CCD at each step and a two-dimensional (2-D) image was assembled from the ensemble of 145 line images resulting in the y-axis resolution of 0.2 mm. The same procedure was performed at seven illumination wavelengths of 666, 696, 730, 770, 806, 846, and 888 nm. The pixel intensity values in the 2-D image were scaled to a normalized dynamic range according to the exposure time. The vertical dark and bright patterns in Fig. 2 due to the channel spatial periodicity were removed by the summation of the pixel data representative of each channel output. This process was equivalent to compressing the image along the x-axis. The image was then processed by a Sobel operator to identify the boundary of the phantom.[38] The positions of the boundaries (as shown in Fig. 2) were then utilized to crop the areas outside the phantom from the image. A statistical approach was used to remove pixels representative of defective channels (e.g., physically blocked) in the cropped image. A defective channel was defined as

$$I_{\text{column\_mean}} < I_{\text{image\_min}} + 0.85 \times (I_{\text{image\_mean}} - I_{\text{image\_min}})$$

and

$$\delta_{\text{column}} < 0.6 \times \delta_{\text{image}}$$

where $I_{\text{column\_mean}}$ and δ_{column} refer to the mean intensity value and the intensity standard deviation of the defective channel across all rows, respectively, and $I_{\text{image\_mean}}$, $I_{\text{image\_min}}$, and δ_{image} refer to the mean intensity value, minimum intensity, and the intensity standard deviation of all the pixels in the image. Once identified, the defective channel was removed by interpolation based on neighboring columns. The last step of image restoration was to remove the nonuniformity in the image due to the variations associated with the illumination

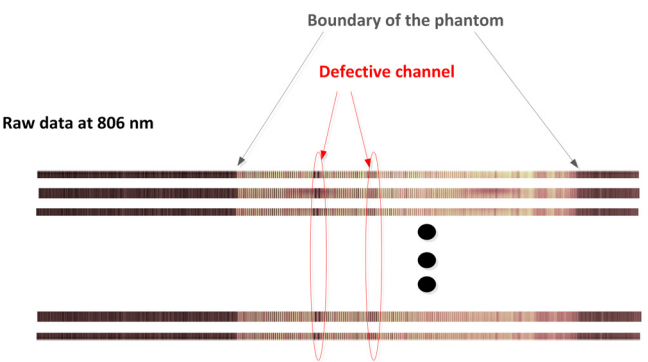

Fig. 2 Raw measurement data at 806 nm of a tissue-mimicking phantom composed of 0.7 wt. % Intralipid®, agarose gel, and indocyanine green (ICG)-containing targets.

beam and AFA channels. It was achieved by normalizing the data along each row according to the mean value of rows where no feature was present.

2.5 *Segmentation*

Further image processing was used to extract the shape of the detected features. The first step was to perform histogram equalization, which effectively increased the image contrast when the signal-to-noise ratio (SNR) was weak. Since six potential features were identified after image restoration, the entire image was divided into six (3×2) regions and each region contained one candidate feature. Histogram equalization was performed locally within each region. This procedure was necessary to account for the large differences in image contrast between shallow targets and deep targets. A modified Otsu segmentation algorithm[38] was applied to the histogram equalized image to group pixels into two classes: zero (0) for target and one (1) for background, which reflected the two types of materials. Segmentation was conducted locally as well using the same region division as used in the histogram equalization process. Since the tissue-mimicking phantom contained absorptive features, a modification to the standard Otsu segmentation program was developed, which skewed the threshold intensity between the two classes toward zero. The seed threshold was set to be the smaller value of $I'_{\text{median}} - 1.5 * \delta'_{\text{image}}$ and $I'_{\text{min}} + \delta'_{\text{image}}$, where I'_{median}, I'_{min}, and δ'_{image} represented the median pixel intensity value, the minimum value, and the standard deviation of the histogram equalized image, respectively.

2.6 *Point Spread Function (PSF) Analysis*

The PSF was estimated to approximate the spatial resolution of the reflectance ADSI images. The PSF was estimated by deconvoluting the binary image obtained at 806 nm with a binary image of the expected shape of the features (reference image). The deconvolution was performed with a regularized filter[39] for each target region separately. The method was validated by recovery of the original image after convolving the reference image with the obtained PSF in 2-D. The measured FWHM of the center peak of the PSF provided an estimate of image spatial resolution.

3 Results and Discussion

3.1 *Raw Images and Impact of Dual Beam Illumination*

A sample raw reflectance ADI result obtained at 806 nm from a 0.7 wt. % Intralipid® phantom is presented in Fig. 2. The periodic bright and dark patterns corresponded to the channel apertures and walls, respectively. The cross-talk between channels was weak as the output from each channel was clearly separated by an intervening shadow due to the intervening channel wall. Signals related to defective channels were corrected during the image restoration process. Special attention was paid to the variations in background illumination in the raw image as the primary objective of introducing dual beam illumination was to minimize such variations. The measured results showed that the variations in background dropped from 40–50% of the dynamic range found in our previous work[4] to 15% in the present work. The increased uniformity in image brightness due to dual beam illumination-aided image restoration resulted in better image segmentation and provided more consistent contrast changes for targets at the same depth [see Figs. 3(a)–3(g)].

3.2 *Image Restoration Results at Different Wavelengths*

Figures 3(a)–3(g) show images at seven different wavelengths recovered from a 0.7 wt. % Intralipid® phantom. The images revealed that the effect of defective channels was successfully

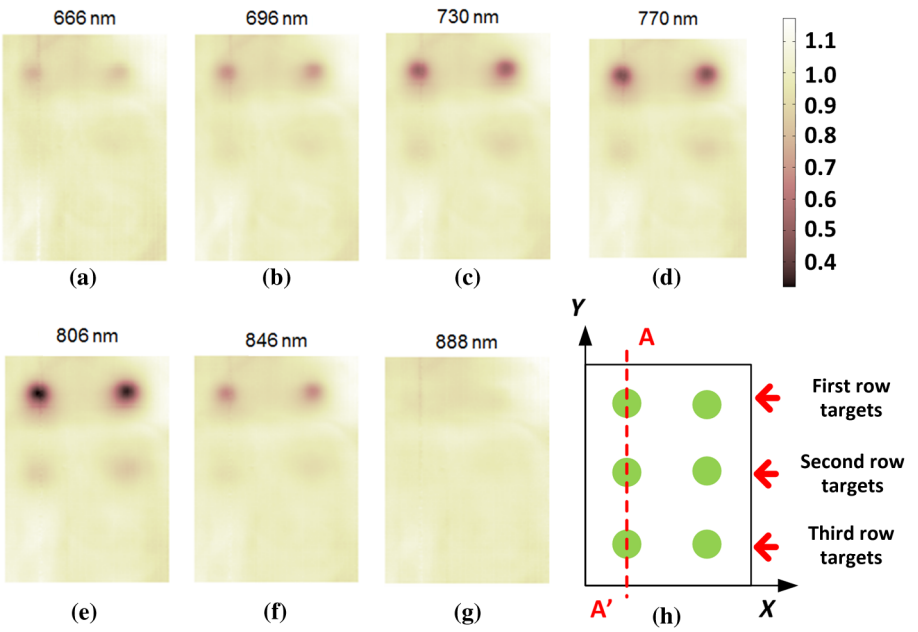

Fig. 3 Multispectral analysis of a tissue-mimicking phantom presented in Fig. 1. The illumination beam was focused on the phantom surface. (a–g) Image restoration results for multispectral images. The color scale represents the transmission intensity in arbitrary units. (h) Schematic of the phantom indicating axes and relative depths of targets.

removed with the approach presented in Sec. 2.4. Consistent with the absorption spectra of 20 μM ICG, targets were detectable from 666 to 846 nm, most distinct at 770 and 806 nm, but undetectable at 888 nm. The light intensity along the line A–A′ in Fig. 3(h) was analyzed and the results are shown in Fig. 4(a). Absorptive features were confirmed at the expected locations of the first, second, and third row targets. To estimate the material composition of the detected features, multispectral analysis was conducted and the absorptive spectral curves are presented in Fig. 4(b). The spectra represent optical density and are compared with a measured 20 μM ICG absorption spectrum (obtained from Ref. 37). It was noted that though the spectral curve shape was close to the ICG curve, the measured spectra were red-shifted. This phenomenon was observed in the previous work as well (see Ref. 5). The primary reason for the red-shift was that at longer wavelengths, scattering in Intralipid® was reduced. Consequently, fewer photons would be diffusively reflected back to the surface, causing a shift of the intensity peak toward longer wavelengths. In addition, the measured spectra were from a mixture of ICG and Intralipid® and the imaging contrast was primarily determined by the ratio between ICG absorption and Intralipid® scattering. The weaker scattering of Intralipid® at longer wavelengths would enhance the contrast as long as the ICG absorption remained high. This would appear as an apparent red-shift in the measured spectra.

3.3 *Image Segmentation Results at Different Wavelengths*

The image restoration and multispectral analysis results described above confirmed that reflectance ADSI could successfully detect shallow absorbers (the first row targets) inside a tissue-mimicking phantom at the peak absorption wavelength and estimate its material composition according to the spectral information. However, identification of deeper targets was more challenging due to the weak SNR. For example, the second and third row ICG targets shown in Figs. 3(a)–3(g) were blurred, and the signal strength (defined as the height of the absorption peak) reduced by ~10× from the first row target to the third row target in Fig. 4(a) at 806 nm while the background noise remained the same. To aid identification in these borderline cases, histogram equalization and segmentation as described in Sec. 2.5 were utilized to identify the target boundary. Each image in Figs. 5(a)–5(g) was divided into three zones corresponding to three rows of targets. The effectiveness of the classification algorithm was examined in terms of the true positive ratio (TPR) and true negative ratio (TNR). The TPR and TNR were calculated by examining pixels one-by-one with respect to the expected location of targets as marked in Fig. 5(h). The TPR was the ratio between the number of on-target pixels, classified as 1, and all known target pixels, while the TNR was the ratio between the number of true off-target pixels, classified as 0, and all known off-target pixels. Both TPR and TNR have an expected value of 1 if the classification was perfect. The TPR and TNR estimates for targets at three different depths at each wavelength are shown in Figs. 6(a) and 6(b). The poorest classification was at 888 nm as both TPR and TNR were extremely low, and the second worst case was at 666 nm as either TPR or TNR or both were low for all targets. For 666 and 888 nm, the algorithm failed to identify targets at all depths, which was expected due to the low absorption of ICG at these wavelengths.

Targets in the first row were successfully recovered at wavelengths between 696 and 846 nm as shown in Figs. 5(b)–5(f). At 806 nm, both TPR and TNR were close to 1 and the recovered shape and size were nearly identical to the expected shape [see Fig. 6(f)]. The classification result obtained at 770 nm for the first row target was the second best overall. At 846 nm, the estimated targets were larger than the expected shape and corresponded to poorer precision than those at 806 and 770 nm. For the second row targets, the geometry was recoverable with reflectance ADSI between 730 and 806 nm. In comparison to the first row deep targets, the TNR did not degrade, but the TPR was reduced, consistent with the fact that a portion of the right-hand target could not be distinguished from the background [Figs. 5(c)–5(e)]. As for the third row of targets, the estimated shape and size of the targets could not be successfully recovered and were reflected in low estimates of the TNR. However, the TPR estimates were comparable to the estimate obtained for the second row of targets. Taken together, the

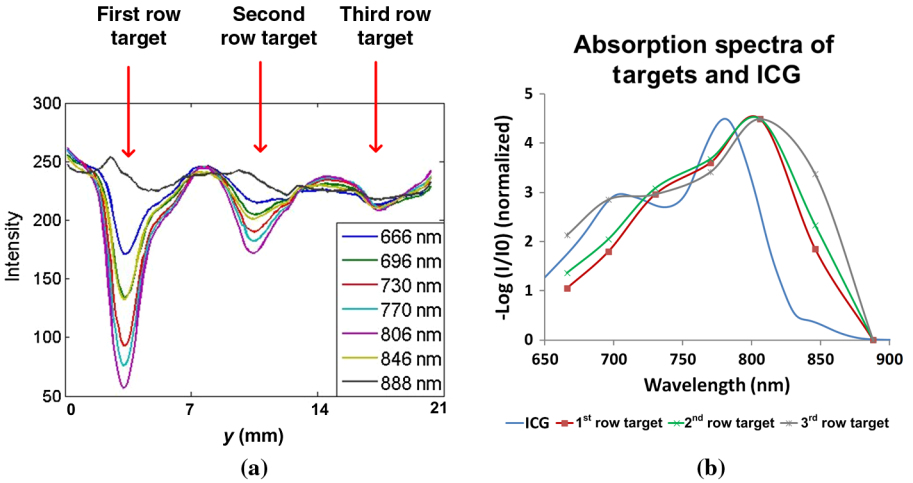

Fig. 4 (a) The spectral responses along A–A′ in Fig. 3(h) in 0.7 wt. % Intralipid® phantom. The illumination beam was focused on the phantom surface. (b) Normalized absorption spectra of three targets versus theoretic 20 μM ICG transmission spectrum after 1 cm^{-1} optical path.

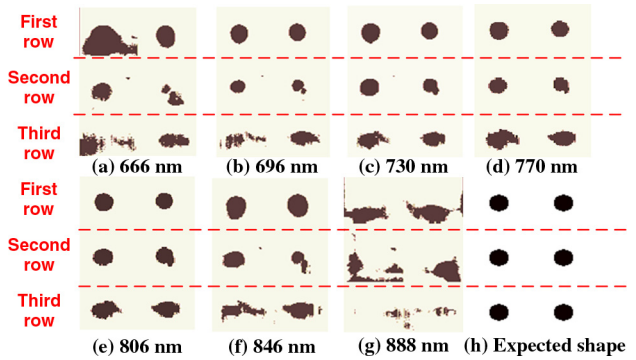

Fig. 5 Histogram equalization and image segmentation results for images presented in Figs. 3(a)–3(g).

results suggested that 3 mm was near the reliable detection limit of reflectance ADSI for a 0.7 wt. % Intralipid® phantom.

3.4 *Impact of Intralipid® Concentration*

A dependence of image brightness on Intralipid® concentration was observed. Figure 7(a) shows an intensity line profile along line A–A′ in Fig. 3(h) at 806 nm for phantoms with 0.7 to 2.0 wt. % Intralipid®. The intensity was normalized according to the exposure time used in each scan. The overall brightness of the image dropped as the concentration increased. For instance, from 0.7 to 1.2 wt. % Intralipid®, brightness dropped by 70% to 80%. To compare image contrast, the measured intensity line profiles were normalized according to the minima at the first row target [Fig. 7(b)]. The contrast of targets increased when Intralipid® concentration increased from 0.7 to 0.9 wt. % and then decreased afterward. Targets at all three rows remained detectable even when the background Intralipid® concentration increased beyond 1.5 wt. % ($\mu_s' \geq 13.6\ \mathrm{cm}^{-1}$). This behavior suggested that the dependence of the number of image-forming photons on the Intralipid® concentration was more complicated for reflectance ADSI than for transmission-based ADSI. Earlier work from our group found that image contrast dropped monotonically as Intralipid® concentration increased during trans-illumination imaging. The effect was attributed to increased scatter and reduced numbers of image-forming quasiballistic photons reaching the detection side of the sample.[5] The biphasic contrast response observed with reflectance ADSI might be related to the fluence-depth profile for a scattering medium, which is expected to have a peak below the surface, where the position and size of the peak are dependent on the scattering level (i.e,. Intralipid® dilution factor). For a target at a fixed depth, a greater number of backscattered photons (i.e., the source of photons available for image formation) would be expected for an intermediate scattering level, where the peak of the fluence-depth profile occurs at a depth greater than the target. In comparison, weaker scattering levels would give fewer image-forming backscattered photons and higher scattering levels would place the peak in-front of the target. In both cases, the apparent image contrast would be lower.

3.5 *Impact of Illumination Focal Depth*

Compared to single point illumination, dual beam illumination was expected to improve image contrast and image brightness. Furthermore, image quality was expected to improve when the illumination beams were focused at an optimal depth. Focusing below the surface had the advantage of preventing specular reflections from entering the detection optics since the illumination beams were limited to two narrow lines physically separated from the line of detection. We performed a series of experiments at three different focal depths (0, 2, and 4 mm) using a phantom with a 1.2 wt. % Intralipid® concentration. The focal depths were selected to be above, at, or below the first row targets with a constant interval. For each illumination scenario, the angle of incidence and location of the illumination beams were left unchanged. Figure 7(c) shows the measured light intensity along A–A′ in Fig. 3(h) at 806 nm. These curves were normalized to their minima at the first row targets [Fig. 7(d)]. Figure 7(c) reveals that the overall brightness of the image dropped as the focal point increased in depth. However, the drop in image brightness was accompanied by an increase in contrast [Fig. 7(d)]. To better understand this behavior, we compared the experiment to the simulation results presented in Refs. 40 and 41, where the absorption density, or the fluence rate transport, T, in a turbid light-scattering medium was simulated, while the focus of the illumination beam was scanned vertically down through the medium. The reference simulations indicated that the fluence delivered to the focal point (i.e., proportional to the background illumination in reflectance ADSI) was reduced substantially when the beam was focused from the sample surface to within one MFP. Beyond

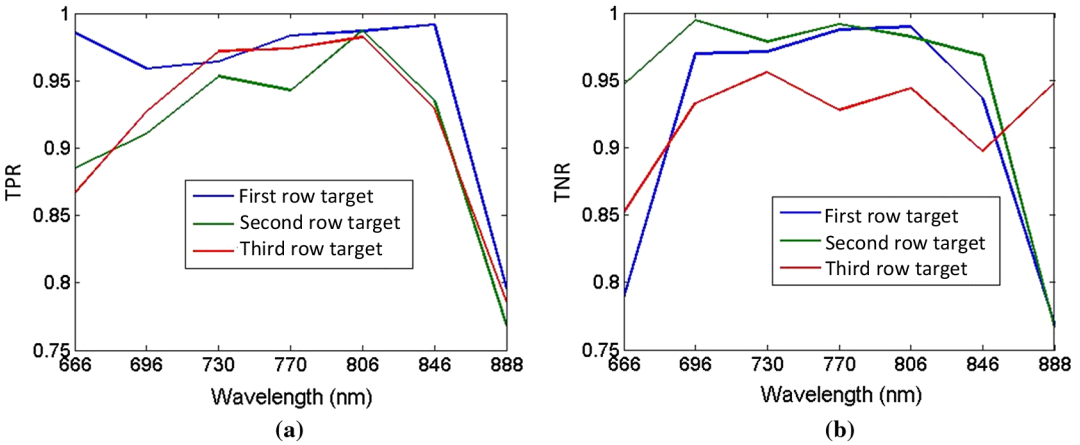

Fig. 6 (a) True positive ratio plot for targets at three different rows shown in Figs. 5(a)–5(g). (b) True negative ratio plot for targets at three different rows shown in Figs. 5(a)–5(g).

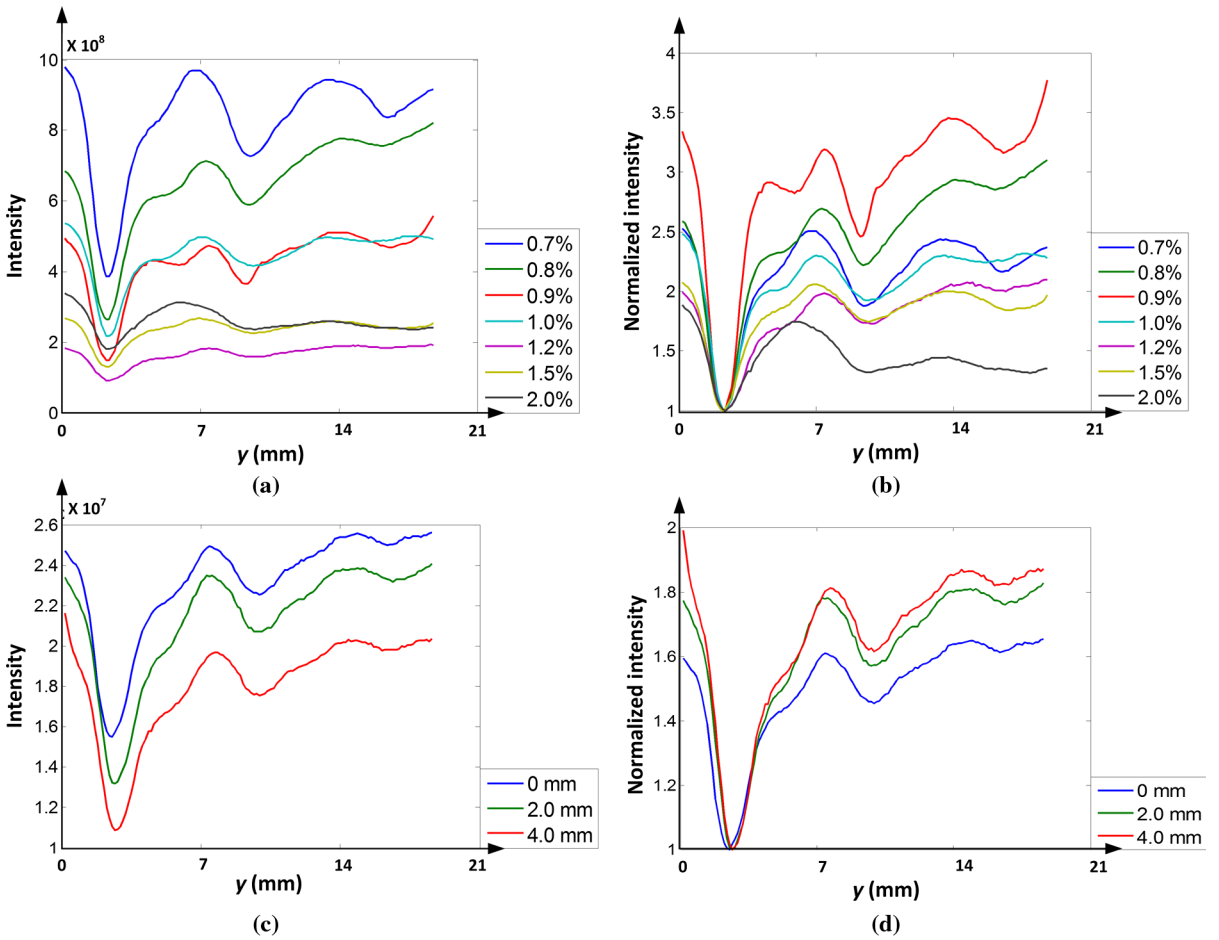

Fig. 7 (a) Intensity line profiles obtained along A–A′ in Fig. 3(h) at 806 nm for multiple phantoms with different Intralipid® concentrations. (b) Normalized curves representative of data in (a). (c) Intensity line profile along A–A′ in Fig. 3(h) for the phantom with 1.2 wt. % Intralipid® background. The focal depth of the illumination beam was 0-, 2-, or 4-mm deep. (d) Normalized curves representative of data in (c).

one MFP, the fluence continued to drop but at a slower rate. On the other hand, the signal intensity reduced while the background illumination source moved deeper and the reduction could be explained by μ_s', which was constant. Therefore, the reported simulation suggested that the image contrast (signal/background) would slightly increase although the overall brightness would drop while the focal depth of the illumination beams increased, which was consistent with our experimental results.

3.6 *Mesoscopic Imaging Capability*

Figures 8(a)–8(d) present the final segmented images for 0.7, 1.0, 1.5, and 2.0 wt. % Intralipid® phantoms at 806 nm. The images represent planar projections, which were expected to reveal features with a lateral dimension equivalent to the full diameter of each spherical target. The first row of targets was resolved in phantoms containing up to 2.0 wt. % Intralipid®, corresponding to an imaging depth of ~2 TMFP (the front surface of the target) or ~4.5 TMFP (the edge of the target in the center). The second row of targets was resolved; however, the edges of each target were not as smooth as those of the first row of targets (at >4 TMFP with 1.5 and 2.0 wt. % Intralipid® phantoms). The third row of targets was resolved for the 0.7 wt. % Intralipid® phantom, but defects were observed along the perimeter of each target. For the 1.0 wt. % Intralipid® phantom, the target shape was distorted. For the 1.5 and 2.0 wt. % Intralipid® phantoms, the targets could not be resolved. The primary reason for the poorer imaging performance for the third row of targets was the weak SNR, and consequently, the increased challenge during the segmentation of the images. In general, the results suggested that reflectance ADSI was capable of imaging objects at 3 TMFP or below and was able to image deeper (up to 4 to 5 TMFP) under certain circumstances.

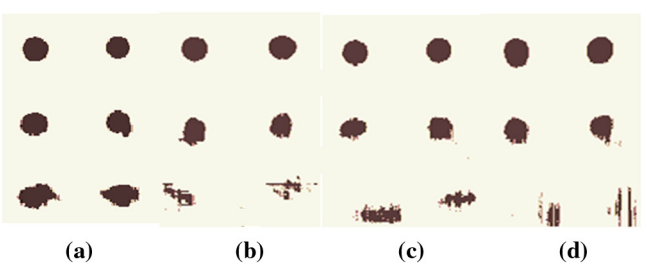

Fig. 8 (a–d) The histogram equalization and image segmentation results for 0.7, 1.0, 1.5, and 2.0 wt. % Intralipid® phantoms at 806 nm.

The spatial resolution of reflectance ADI has been examined in earlier work for a moderately scattering medium (see Ref. 4), where a series of metallic L-shaped targets were imaged. This earlier work demonstrated that reflectance ADI could resolve L-shaped targets with lines and spaces of about 0.2 mm at

approximately 1 TMFP. For images acquired with reflectance ADSI in this work, spatial resolution was limited by both instrument capability and sample properties. The instrument capability was determined by AFA geometry, the scanning step size, and the camera resolution, which were 0.1 mm (channel periodicity), 0.2 mm, and 8 μm (along the longitudinal axis of the AFA), respectively. Therefore, we expected the image resolution limited by the reflectance ADSI setup to be better than 1 mm, but poorer than 0.2 mm.

The spatial resolution is also affected by the structure and the optical properties of the sample and can be estimated from the PSF. In real tissue samples with natural chromophores, heterogeneity, and high levels of scattering, the resolution will drop as the depth increases and the PSF will be wider with stronger noise levels. The estimate of the PSF was calculated based on the shapes of the targets as shown in Fig. 5(e) and the expected shape as shown in Fig. 5(h). The results are presented in Fig. 9. For the first row targets, the PSF estimates suggested that the spatial resolution was about 0.4 mm. For the second row targets, the computed PSFs showed that the resolution was poorer in the x-direction at approximately 0.6 mm. For the third row targets, the central peak of the PSF was not measurable and the spatial resolution of the image could not be properly evaluated. Taken together, the previous work on reflectance ADI in combination with the current phantom results, led us to conclude that reflectance ADSI could provide submillimeter spatial resolution for targets at a depth up to 3 to 4 TMFP. Compared to transillumination ADSI whose spatial resolution is on the order of 200 μm at ~5 TMFP, reflectance ADSI has poorer spatial resolution due to the folding of the optical path.[42]

The field-of-view of reflectance ADSI is determined by the AFA dimensions and the scanning process. The exposure time at each scanning step was approximately 5 s to ensure that the obtained signal intensity was sufficient. With 0.2 mm in scanning step and 2.5 cm in AFA length (x-direction), this technique could produce a 2.5 cm × 3.0 cm image in roughly 3 min in the current setup at one wavelength or a hyperspectral image with an imaging spectrometer.

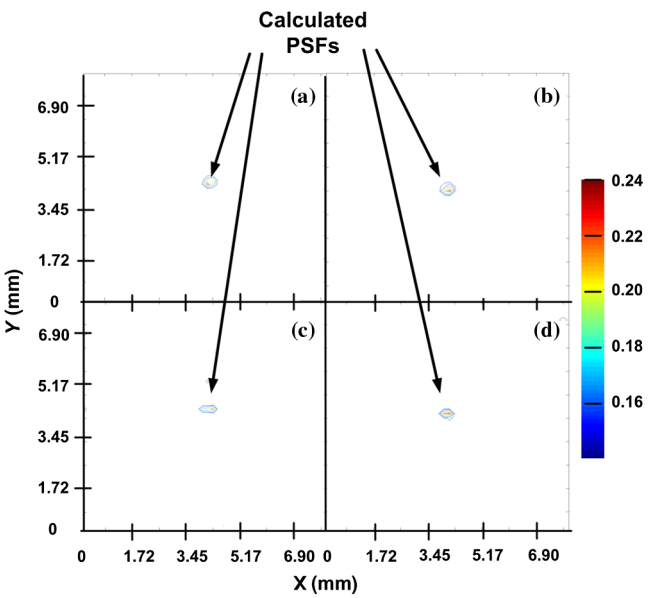

Fig. 9 (a–d) Calculated point spread functions (PSFs) for objects in Fig. 5(e) from top left to middle right. Noise with less than half of the peak signal amplitude or away from the center is not presented. Calculated PSFs for bottom two objects are noisy and are not shown.

In general, reflectance ADSI is able to provide submillimeter resolution for features up to 3 to 4 TMFP with the field-of-view of a couple of square centimeters. In comparison, LOT has demonstrated spatial resolution of 200 μm over the depths of 3 to 5 TMFP with the field-of-view of 3 mm × 3 mm in sample applications such as imaging studies of the cortical hemodynamics and neurophysiology in the rat.[22,23] SFDI provides a field-of-view of several centimeters in length and width, with an imaging depth of 2 TMFP and submillimeter spatial resolution. It is currently practiced for evaluation and diagnosis of large skin abnormalities or wide-field optical imaging of breast pathology *in situ*.[24–26] MSOT yields spatial resolution of the order of 50 to 200 μm for imaging up to 10 TMFP at the expense of high cost and instrument complexity. Reported applications include imaging blood vessels, the kidneys, the liver, and the gall bladder in mice and adult zebrafish.[27,28,30,32] In the limited results reported for BGSI, the technique demonstrated <1 mm spatial resolution at a depth penetration of 1 to 1.5 TMFP with a field-of-view of 10 mm × 10 mm for the samples such as SCID or athymic nude mice with human melanoma xenografts.[19,21] Overall, there is no question that MSOT provides the best performance, but modalities such as reflectance ADSI, LOT, SFDI, and BGSI offer viable alternatives depending on the resolution and depth penetration requirements. Reflectance ADSI is an attractive modality since it inherently does not depend on an image reconstruction process. In addition, the reflectance ADSI provides a relatively large field-of-view with reduced instrumental complexity and cost as it does not require a coherent light source, a reference beam, optical sectioning, or source–detector arrays. Furthermore, reflectance ADSI offers spectroscopic imaging capabilities for material characterization. All of these features suggest that reflectance ADSI might find a niche as a diagnostic tool for optical imaging of subcutaneous targets in the mesoscopic domain.

3.7 *Application of Reflectance ADSI and its Limitations*

Review of the work described in Refs. 8, 18, 43–45 suggested that the reduced scattering coefficients of human skin, including epidermis, dermis, and subcutaneous fat are expected to be within the range of 9 to 40 cm^{-1} in the spectral range from 600 to 900 nm, which are similar to the optical properties of the tissue-mimicking phantoms employed. Analysis conducted in Ref. 2 also suggested that 1-mm thick 1.0 wt. % Intralipid® phantom had a scattering level equivalent to 1-mm thick soft tissue. In addition, the absorption coefficient of human skin has been reported to be typically < 1 cm^{-1} (Refs. 8, 9, and 43) and blood is known to have an absorption coefficient that is up to two to three orders of magnitude larger between 600 and 700 nm due to hemoglobin.[46] Based on these estimates above, the attenuation due to blood vessels near the skin is comparable to the attenuation observed from ICG and Intralipid® in the tissue-mimicking phantoms. Therefore, reflectance ADSI should be capable of noninvasive imaging of subcutaneous vasculature that feed skin tumors, which are also the typical targets of other mesoscopic imaging modalities. In addition, reflectance ADSI is expected to be implemented in other typical mesoscopic imaging applications as presented in Sec. 1.3. The current setup has yet to be tested for applications involving *in vivo* imaging as the line scan process is still relatively slow. The two-dimensional

AFA proposed in Ref. 42 would eliminate the time-consuming scan process and will enable the capture of an image at one wavelength band during a single exposure. With a fast spectral scanner, real-time tissue imaging and spectral analysis will be achievable, which may facilitate the detection and identification of skin lesions.[47,48]

In comparison to earlier work, our results demonstrated that the dual illumination setup was capable of generating uniform background illumination, which resulted in improved image contrast. Furthermore, the measurement result in Sec. 3.5 led us to conclude that the illumination beam should be focused as deeply as possible and as long as the overall brightness was sufficient for detection. However, even with these improvements, the depth penetration of reflectance ADSI is still expected to be <5 TMFP and the spatial resolution to be poorer than 200 μm in skin tissues due to the inherently weak SNR.

Our multispectral analysis method only utilized seven wavelength bands. Although the analysis was effective with strongly absorbing targets, better spectral resolution would likely be required for accurate identification of the material composition of targets in tissue imaging applications, where targets are likely to be more complex in shape and spectral responses, and of lower optical absorption. In these more difficult cases, hyperspectral analysis implemented with a spectrometer may prove to be superior.

4 Conclusions

This paper has presented the developments in reflectance ADSI, a reflectance-based technique for optical imaging in the mesoscopic domain. The work utilized tissue-mimicking phantoms with absorptive targets to evaluate the AFA-based setup. Image restoration and segmentation of reflectance ADSI data resulted in successful identification of absorptive targets 3 mm in diameter and up to 3 to 4 TMFP below the surface of phantoms composed of 0.7 to 2.0 wt. % Intralipid® and agarose gel. The spatial resolution was <1 mm and the field-of-view was 2.5 cm × 3.0 cm. In addition, multispectral analysis successfully extracted the absorption spectra of the targets according to the measured intensity at the target locations. The spectra of the detected ICG-loaded targets were similar to absorption spectra of ICG. The relationships between image brightness, image contrast, Intralipid® concentration, and the focal depth of the illumination beams were measured. The results confirmed that the reflectance ADSI was able to detect absorptive targets (such as 20 μM ICG) embedded in a scattering medium representative of human skin. Due to its low cost and simple implementation, reflectance ADSI could be considered as a potential biomedical tissue scanning solution for subcutaneous optical abnormalities. Future work could include the implementation of hyperspectral detection and principle component analysis to examine whether reflectance ADSI can accurately identify absorbers inside more complex turbid media. The influence of the illumination angle and the distance between the illuminators also needs additional investigation. However, a prudent next step should be to test reflectance ADSI on a sample with unknown optical properties and validate the results via other methods. The capability of reflectance ADSI to image tissues with both heterogeneous scattering and absorptive properties should also be explored. In order to be successful as a biomedical imaging tool, reflectance ADSI needs an image restoration process to validate the existence of absorptive features and a segmentation process to recover the shape of the targets. Future work should focus on studying the susceptibility of these algorithms to noise. New segmentation algorithms could also be developed for situations where there are more than two types of materials inside the imaged volume.

Acknowledgments

This project was funded by grants from Natural Sciences and Engineering Research Council of Canada (NSERC) to Jeffrey J.L. Carson and Bozena Kaminska. Yan Zhang was supported by NSERC and British Columbia Innovation Council, Natural Resources and Applied Science (BCIC NRAS) grants. Fartash Vasefi was supported by a London Regional Cancer Program Translational Breast Cancer Research Trainee Fellowship. E. Ng was supported by a Natural Sciences and Engineering Research Council of Canada via Canadian Graduate Student—Master award. The authors wish to gratefully acknowledge the Nanofabrication Facility at the University of Western Ontario for the fabrication of the AFA.

References

1. F. Vasefi et al., "Image contrast enhancement in angular domain optical imaging of turbid media," *Opt. Express* **16**(26), 21492–21504 (2008).
2. F. Vasefi et al., "Transillumination hyperspectral imaging for histopathological examination of excised tissue," *J. Biomed. Opt.* **16**(8), 086014 (2011).
3. F. Vasefi et al., "Angular domain transillumination imaging optimization with an ultrafast gated camera," *J. Biomed. Opt.* **15**(6), 061710 (2010).
4. F. Vasefi et al., "An optical imaging technique using deep illumination in the angular domain," *IEEE J. Sel. Top. Quantum Electron.* **13**(6), 1610–1620 (2007).
5. F. Vasefi et al., "Angular domain fluorescence imaging for small animal research," *J. Biomed. Opt.* **15**(1), 016023 (2010).
6. F. Vasefi et al., "Transmission and fluorescence angular domain optical projection tomography of turbid media," *Appl. Opt.* **48**(33), 6448–6457 (2009).
7. F. Vasefi et al., "Angular domain spectroscopic imaging for breast cancer margin assessment after lumpectomy," *Proc. SPIE* **8220**, 822003 (2012).
8. R. R. Anderson and J. A. Parrish, "The optics of human skin," *J. Invest. Dermatol.* **77**(1), 13–19 (1981).
9. A. P. Dhawan, B. D'Alessandro, and X. Fu, "Optical imaging modalities for biomedical applications," *IEEE Rev. Biomed. Eng.* **3**, 69–92 (2010).
10. A. M. Zysk et al., "Optical coherence tomography: a review of clinical development from bench to bedside," *J. Biomed. Opt.* **12**(5), 051403 (2007).
11. A. F. Fercher, "Optical coherence tomography—principles and applications," *Rep. Prog. Phys.* **66**(2), 239–303 (2003).
12. R. Wang et al., "Megahertz streak-mode Fourier domain optical coherence tomography," *J. Biomed. Opt.* **16**(6), 066016 (2011).
13. H. Skvara et al., "In vivo fluorescence confocal microscopy: indocyanine green enhances the contrast of epidermal and dermal structures," *J. Biomed. Opt.* **16**(9), 096010 (2011).
14. R. Orzekowsky-Schroeder et al., "In vivo spectral imaging of different cell types in the small intestine by two-photon excited autofluorescence," *J. Biomed. Opt.* **16**(11), 116025 (2011).
15. P. Zakharov et al., "Dynamic laser speckle imaging of cerebral blood flow," *Opt. Express* **17**(16), 13904–13917 (2009).
16. M. A. O'Leary et al., "Experimental images of heterogeneous turbid media by frequency-domain diffusing-photon tomography," *Opt. Lett.* **20**(5), 426–428 (1995).
17. T. Durburan et al., "Diffuse optics for tissue monitoring and tomography," *Rep. Prog. Phys.* **73**(7), 076701 (2010).
18. V. Ntziachristos, "Going deeper than microscopy: the optical imaging frontier in biology," *Nat. Methods* **7**(8), 603–614 (2010).
19. Z. Xu, A. K. Somani, and Y. L. Kim, "Scattering anisotropy-weighted mesoscopic imaging," *J. Biomed. Opt.* **17**(9), 090501 (2012).

20. C. Vinegoni et al., "In vivo imaging of Drosophila melanogaster pupae with mesoscopic fluorescene tomography," *Nat. Methods* **5**(1), 45–47 (2007).
21. Z. Xu et al., "Back-directional gated spectroscopic imaging for diffuse light suppression in high anisotropic media and its preclinical applications for microvascular imaging," *IEEE J. Sel. Top. Quantum Electron.* **16**(4), 815–823 (2010).
22. E. M. C. Hillman et al., "Laminar optical tomography: demonstration of millimeter-scale depth-resolved imaging in turbid media," *Opt. Lett.* **29**(14), 1650–1652 (2004).
23. S. A. Burgess et al., "Simultaneous multiwavelength laminar optical tomography," *Opt. Lett.* **33**(22), 2710–2712 (2008).
24. A. M. Laughney et al., "Spectral discrimination of breast pathologies in situ using spatial frequency domain imaging," *Breast Cancer Res.* **15** (4), R61 (2013).
25. J. R. Weber et al., "Multispectral imaging of tissue absorption and scattering using spatial frequency domain imaging and a computed-tomography imaging spectrometer," *J. Biomed. Opt.* **16**(1), 011015 (2011).
26. K. P. Nadeau et al., "Quantitative assessment of renal arterial occlusion in a porcine model using spatial frequency domain imaging," *Opt. Lett.* **38**(18), 3566–3569 (2013).
27. R. Ma et al., "Multispectral optoacoustic tomography (MSOT) scanner for whole-body small animal imaging," *Opt. Express* **17**(24), 21414–21426 (2009).
28. A. Taruttis et al., "Fast multispectral optoacoustic tomography (MSOT) for dynamic imaging of pharmacokinetics and biodistribution in multiple organs," *PLoS One* **7**(1), e30491 (2012).
29. K. M. Cross et al., "Clinical utilization of near-infrared spectroscopy devices for burn depth assessment," *Wound Repair Regener.* **15**(3), 332–340 (2007).
30. H. F. Zhang et al., "Functional photoacoustic microscopy for high-resolution and noninvasive in vivo," *Nat. Biotechnol.* **24**(7), 848–851 (2006).
31. J. Sharpe et al., "Optical projection tomography as a tool for 3D microscopy and gene expression studies," *Science* **296**(5567), 541–545 (2002).
32. D. Razansky et al., "Multispectral optoacoustic tomography of deep-seated fluorescent proteins in vivo," *Nat. Photonics* **3**(7), 412–417 (2009).
33. S. T. Flock et al., "Optical properties of intralipid: a phantom medium for light propagation studies," *Laser. Surg. Med.* **12**(5), 510–519 (1992).
34. H. Ding et al., "Determination of refractive indices of porcine skin tissues and intralipid at eight wavelengths between 325 nm and 1557 nm," *J. Opt. Soc. Am. A* **22**(6), 1151–1157 (2005).
35. S. Jacques, "Optical properties of 'Intralipid™', an aqueous suspension of lipid droplets," http://omlc.ogi.edu/spectra/intralipid/index.html, Oregon Medical Laser Center (1998).
36. A. N. Bashkatov et al., "Optical properties of human skin, subcutaneous and mucous tissues in the wavelength range from 400 to 2000 nm," *J. Phys. D* **38**(15), 2543–2555 (2005).
37. S. Prahl, "Optical absorption of indocyanine green (ICG)," http://omlc.ogi.edu/spectra/icg/index.html, Oregon Medical Laser Center (2012).
38. R. C. Gonzales and R. E. Woods, *Digital Image Processing*, 3rd ed., Pearson/Prentice Hall, Harlow (2008).
39. S. S. Al-amri and N. V. Kalyankar, "A comparative study for deblured average blurred images," *Int. J. Comput. Sci. Eng.* **2**(3), 731–733 (2010).
40. L. V. Wang and G. Liang, "Absorption distribution of an optical beam focused into a turbid medium," *Appl. Opt.* **38** (22), 4951–4958 (1999).
41. S. Jacques, "Confocal microscopy," http://omlc.ogi.edu/animation/FfocusScatt.html, Oregon Medical Laser Center (2012).
42. E. Ng and J. J. L. Carson, "Resolution analysis of an angular domain imaging system with two dimensional angular filters," *Proc. SPIE* **8579**, 857913 (2013).
43. A. N. Bashkatov et al., "Optical properties of human skin, subcutaneous and mucous tissues in the wavelength range from 400 to 2000 nm," *J. Phys. D* **38**(15), 2543–2555 (2005).
44. E. Salomatina et al., "Optical properties of normal and cancerous human skin in the visible and near-infrared spectral range," *J. Biomed. Opt.* **11**(6), 064029 (2006).
45. M. J. C. Van Gemert et al., "Skin optics," *IEEE Trans. Biomed. Eng.* **36**(12), 1146–1154 (1989).
46. S. Prahl, "Optical absorption of hemoglobin," http://omlc.ogi.edu/spectra/hemoglobin/index.html, Oregon Medical Laser Center (1999).
47. I. Diebele et al., "Analysis of skin basalioma and melanoma by multispectral imaging," *Proc. SPIE* **8427**, 842732 (2012).
48. D. Kapsokalyvas et al., "Spectral morphological analysis of skin lesions with a polarization multispectral dermoscope," *Opt. Express* **21**(4), 4826–4840 (2013).

Yan Zhang obtained his master of applied science degree from Simon Fraser University and bachelor's of science degree from Tsinghua University. Recently, he received his PhD degree from Simon Fraser University. His research interests include angular domain spectroscopic analysis and imaging, nanostructures for sensing and optical filtration, and the reliability of LED lighting products.

Fartash Vasefi received his PhD degree in biomedical engineering from Simon Fraser University, Canada, in 2010. Currently, he is a research scientist at the Spectral Molecular Imaging Inc. After a postdoctoral fellowship at the Lawson Health Research Institute, he joined SMI in 2012 where his interests are in commercially adoptable technologies that use multimode optical imaging systems, novel image processing methods, and integrated micrometer and nanometer scale optical devices in biological sensing and imaging systems.

Eldon Ng obtained a master's degree in medical biophysics from the University of Western Ontario. He is currently pursuing an MD degree at the Queen's University School of Medicine. His research focuses on developing angular domain imaging for biological tissues.

Astrid Chamson-Reig studied biology at the University of Buenos Aires, Argentina, where she completed her PhD degree in 1999 in physiology and endocrinology of reproduction. She pursued postdoctoral positions at Lawson Health Research Institute in London, Ontario, Canada, in Diabetes and Metabolism and Lawson Imaging programs. She has been a research coordinator at Lawson since 2012, with Dr. Jeffrey Carson, providing support to his research in optics and photoacoustic imaging and managing students in the laboratory.

Bozena Kaminska is currently a professor at Simon Fraser University and a Canada research chair. She serves as a director and chief scientific officer for NanoTech Security Corp, and is a chair of the Board of Directors of CMC Microsystems. She is a prolific inventor with major contributions to science; four successful spin-off companies have resulted from her research. She holds multiple patents and has authored more than 300 peer-reviewed publications in top scientific journals.

Jeffrey J. L. Carson is an imaging scientist at the Lawson Health Research Institute in London, Ontario, Canada. His research group develops new methods for fast optical imaging with emphasis on 3-D photoacoustic imaging, time-gated imaging, and techniques that utilize nanostructures as sensing elements. He holds national funding awards from the Canadian Institutes of Health Research, the Natural Sciences and Engineering Research Council of Canada, and the Canada Foundation for Innovation.